

Performance of the SOAR Speckle Instrument

ANDREI TOKOVININ¹

¹*Cerro Tololo Inter-American Observatory — NFSs NOIRLab Casilla 603, La Serena, Chile*

ABSTRACT

The High Resolution Camera (HRCam) speckle imager at the 4.1 m Southern Astrophysical Research telescope is a highly productive instrument that has accumulated about 40K observations to date. Its performance (detected flux, level of the speckle signal, signal-to-noise ratio, and limiting magnitude) is studied here using both the actual data and realistic simulations, including the detector noise. In the calculation of the speckle power spectrum, signal clipping is essential to reduce the noise impact and maximize the sensitivity. Increasing exposure time of individual frames beyond 30 ms does not improve the limiting magnitude, which ranges from 11.5 to 14 mag under a seeing from 1''6 to 0''6 in the wide-band *I* filter. A gain of at least one magnitude is expected if the current electron multiplication CCD is replaced by a high-end CMOS detector with a subelectron readout noise. This study will help in planning, executing, and automating future speckle observations with HRCam and other speckle imagers.

Keywords: binaries:visual

1. INTRODUCTION

Speckle interferometry, introduced by Labeyrie (1970), has become a standard method of high-resolution observations at optical wavelengths, complementing adaptive optics in the infrared. At that time, recording and processing of a large number of images with short exposure and fine pixel scale presented a formidable technical challenge. With the advent of modern computers and electron multiplication (EM) CCDs, however, speckle interferometry has become a technically feasible and efficient technique (Tokovinin & Cantarutti 2008; Horch et al. 2009). Nowadays, appearance of low-noise CMOS detectors challenges the dominant role of EM CCDs in speckle interferometry and opens new horizons. The principles of speckle interferometry are covered in numerous textbooks and papers, e.g. by Goodman (1985).

Speckle interferometry serves mostly for the study of orbital motions of binary and multiple stars, for surveys of binarity in various stellar samples, and for screening exoplanet hosts for close companions. Speckle instruments based on EM CCDs are in active use, e.g. the DSSI (Horch et al. 2009; Davidson et al. 2024),

the twin speckle cameras at Gemini (Scott & Howell 2018; Scott et al. 2021), the Quad speckle camera at the 4 m Lowell Discovery Telescope (Clark et al. 2024), and the speckle instrument of the 6 m telescope (Mitrofanova et al. 2021). The Gaia mission (Gaia Collaboration et al. 2016, 2021) is a powerful driver of current and future speckle programs that provide an essential complement to Gaia.

The High Resolution Camera (HRCam) has been used at the Southern Astrophysical Research (SOAR) 4.1 m telescope in Chile since 2007. It has been a very productive and low-maintenance instrument for speckle interferometry (see Mason et al. 2023, and references therein). In 2017, the detector was upgraded to an iXon EM CCD with a high quantum efficiency and low noise (Tokovinin 2018). HRCam uses 10–15 nights per year and typically covers 300 targets in a night. To date (2024 May), there are 40,776 accumulated speckle observations of 16,319 targets (measurements of binary stars and nonresolutions) — one of the largest speckle data sets in the world. A brief review of the scientific use of the HRCam data can be found in Tokovinin (2018).

So far, the performance of HRCam received little attention; all efforts have been devoted to the observations. Our goal here is to quantify the quality of the speckle data by such parameters as speckle contrast and signal-to-noise ratio (SNR) and to study their depen-

dence on the observing conditions and instrument parameters. Estimates of the expected SNR will help in planning future observations by setting acceptable conditions for each target. Eventually, the data quality prediction and control will enable automation of the observations, which, so far, largely depend on the observer’s expertise. An additional motivation is to evaluate the potential gain in sensitivity offered by an upgrade to a high-end CMOS detector.

In Section 2, the requisite information on HRCam is assembled, including the detector parameters, data processing, and photometric calibration. Simulations are covered in Section 3, quantifying the impact of finite exposure time and spectral bandwidth and the role of the detector noise. The simulation code is described in the Appendix. Based on the simulations, the benefit of upgrading to a CMOS detector is explored in Section 4. The perspective of automating speckle interferometry in the future is briefly discussed in Section 5, and the results are summarized in Section 6.

2. PERFORMANCE OF HRCAM AT SOAR

The HRCam speckle camera and its data processing have been covered by Tokovinin (2018). Here, the main instrument parameters are recalled for consistency, and its photometric calibration is given. In the following Section, this information is used for comparison with simulations.

2.1. Instrument Parameters

Since 2017, the EM CCD detector iXon X3 888 from Andor¹ has been in use in HRCam. The optical magnification has been adjusted to project its 13 μm square pixels at a scale of $p = 0''.01575$ per pixel on the sky to sample the diffraction-limited speckles adequately. For a telescope diameter $D = 4.1$ m, the critical sampling of $\lambda/(2D)$ corresponds to a pixel scale of $0.0135''$ and $0.0207''$ at a wavelength λ of 540 and 822 nm, respectively, corresponding to the two most used spectral bands. The speckle image is slightly undersampled in the green filter y and oversampled in the I band by 1.3 times.

The iXon camera has a conversion factor of $g = 10.1$ electrons (e-) per Analog to Digital Unit (ADU), as specified by the vendor and confirmed by our measurements. The EM gain E_g setting corresponds to the actual signal amplification, to within a few per cent. The rms readout noise (RON) is 4.5 ADU or 45 e-, and its impact becomes negligibly small at $E_g > 100$. A typical histogram of the dark signal shows a Gaussian distribu-

tion with the width that characterizes the RON and an exponential tail produced by the single-electron events (see Figure 3 in Tokovinin 2018). These clock-induced charge (CIC) events do not depend on the exposure time (the dark current is negligibly small because the CCD is cooled to -60°C), and their rate is quantified by the fractional area of the exponential tail in the dark-signal histogram; it is about 0.02 events per pixel per frame. In this camera, the CIC rate depends on the vertical clock time, which has been chosen to minimize the rate. Parameters of the detector, remeasured in 2023, show no degradation relative to our measurements in 2016, despite its intensive use for 7 yr.

2.2. Data Acquisition and Processing

So far, the operation of HRCam relies on the human experience and on the quick-look evaluation of results immediately after acquisition. The targets are selected flexibly, depending on the observing conditions. Most HRCam data are acquired in the standard mode, with a 200×200 pixels region of interest (ROI), 400 images per data cube, without binning. The field of view, $3''.15$, is large enough to capture seeing-limited images without truncation. The minimum exposure time in this mode is 24.4 ms, and the effective exposure time (interval between successive images) is 27.9 ms. Acquisition of a standard data cube thus takes 12 s, and two cubes per observation are normally recorded with an EM gain of $E_g = 100$. These parameters are adopted in the simulations. Faint targets are observed in the I filter; its transmission and the detector spectral response define the bandwidth with an average wavelength of 822 nm and a width of 140 nm. Note, however, that both parameters depend on the stellar temperature, and the effective response becomes “redder” for red stars. The y filter (543/22 nm) is used for observations of bright and close binaries with maximum angular resolution.

The standard speckle interferometry (Labeyrie 1970) is based on the evaluation of the *speckle power spectrum* (PS) P , which is the average square modulus of the Fourier transform (FT) of each image I_i in the data cube:

$$P(\mathbf{f}) = \frac{1}{N_z} \sum_{i=1}^{N_z} |\tilde{I}_i(\mathbf{f})|^2, \quad (1)$$

where \mathbf{f} is the spatial frequency, N_z is the number of frames in the data cube, and tilde denotes the FT operator. From each data cube, the speckle pipeline creates four two-dimensional images: the PS, the speckle autocorrelation function (ACF), which is the inverse FT of the PS, the shift-and-add (SAA) or “lucky” image registered on the brightest pixels, and the average image with correction of the overall image centroid motion;

¹ www.andor.com

see details and illustrations in Tokovinin (2018) and in Figure 1.

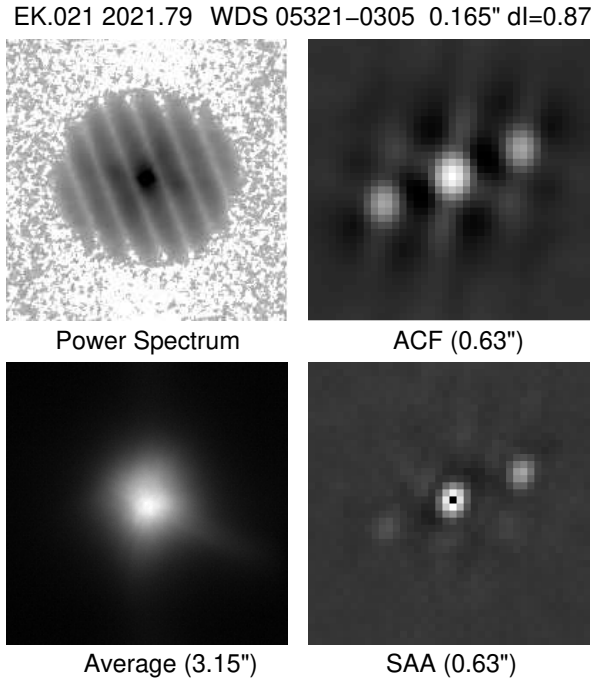


Figure 1. Example of processing the data cube EK.021 recorded on 2021.79. The binary star WDS 05321–0305 (separation $0''.165$, $\Delta I = 0.87$ mag) was observed in the I filter with standard parameters (ROI 200×200 pixels, exposure time 24 ms, 400 frames per cube). The speckle PS is shown in negative logarithmic stretch. The central 40×40 pixels ($0''.63$) fragments of the ACF and SAA images are displayed. The FWHM of the average image is $0''.58$. Under good seeing, residual aberrations of the telescope are manifested as asymmetric details of the average image, as a cross-like feature in the PS, and as faint spurious details in the ACF.

The algorithm of the PS calculation has been “trained” on the real data to enhance the speckle signal from faint sources. It is illustrated in Figure 2. The average number of CIC events in a 200×200 frame, 800, becomes comparable to the number of detected stellar photons N_{ph} for faint stars, seriously degrading the sensitivity. After subtraction of the bias (i.e. the average image taken without illumination), most pixels are empty, containing only the RON, while some pixels contain the speckle and CIC signals (a). To reduce the effect of RON, the signal is clipped at the level of 10 ADU, and all pixels below this level are set to zero (b). The first clipping still transmits the CIC events, which affect calculation of the image centroid and flux for faint stars. So, the clipped signal is smoothed with a 5-pixel square kernel, and the second threshold equal to the 0.3 fraction of its maximum is defined (c). It is subtracted from the smoothed signal, negative pixels are set to zero, and the

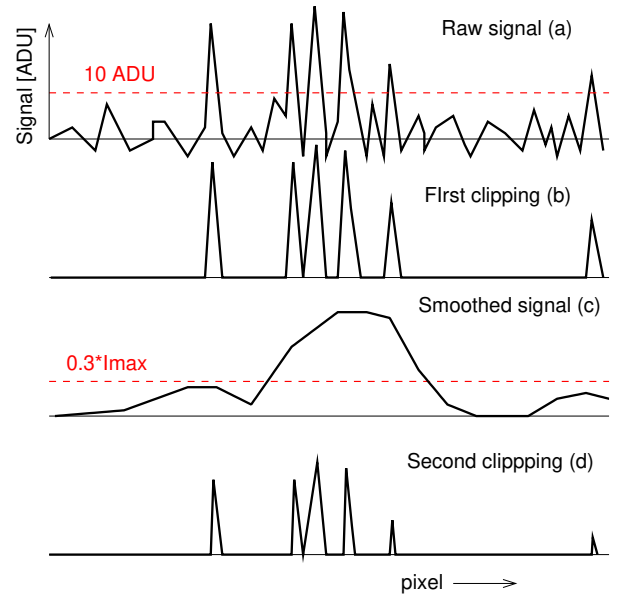


Figure 2. Illustration of the standard signal processing in HRCam. Signal in a single row of the bias-subtracted image at various processing stages is plotted by thick black lines, the thresholds are shown in red; see the text.

clipped smoothed image is used for the centroid calculation to produce the average tilt-corrected image. The second threshold is also subtracted from the clipped signal (b), and the resulting nonnegative image (d) is used to calculate the PS and SAA. The sum of the doubly clipped image (d) is less than the sum of the original bias-subtracted image (a) by a large (~ 7) factor, so the fluxes estimated from the clipped images are severely biased.

The simulations described below confirm that the current algorithm produces near-optimum results for faint stars. However, calculation of the PS does not need the second clipping, and the image (b) can be used instead. It is important, however, to subtract from it the average background because the PS is normalized by its value at zero spatial frequency f , which equals the square of the total flux. For correct evaluation of the speckle power, only the stellar flux must be used for normalization, so the average background must be subtracted from the clipped image in (b) before calculation of the FT and summation of its square modulus over all frames in the cube. Otherwise, the CIC background contributes to the flux, producing a spike in the PS at $f = 0$. The second clipping used in the standard algorithm reduces the background effect but does not cancel it completely. So, the original algorithm of the PS calculation was modified to use only single clipping with background subtraction. Other data products (average and SAA images) are still derived from the doubly clipped images.

2.3. Photometric Calibration of HRCam

During 2022–2023, a large number of red dwarfs from the Gaia Catalog of Nearby Stars (GCNS) were observed with HRCam (Tokovinin 2023). Parameters of 1325 such observations (flux, exposure time, EM gain, and coordinates) were retrieved from the general speckle database and matched to the GCNS sources to get their photometry (magnitudes in the Gaia G , G_{BP} , and G_{RP} bands). Fluxes in the database, strongly biased by the image clipping (see above), were replaced by fluxes measured on the saved average images.

Given the measured flux F in ADU per frame, the conversion factor $g = 10.1$ e- per ADU, the exposure time t in seconds, and the EM gain E_g , the instrumental magnitudes of HRCam m_{inst} are computed as

$$m_{\text{inst}} = 25 - 2.5 \log_{10}[gF/(tE_g)]. \quad (2)$$

The offset of 25 mag is arbitrary. The spectral response of HRCam in the I filter is “redder” compared to the Gaia G band, so the difference between instrumental magnitudes and G depends on the $G_{BP} - G_{RP}$ color of the star. This empirical dependence can be approximated by the linear formula

$$m_{\text{inst}} \approx G - 0.61 - 0.35 (G_{BP} - G_{RP}). \quad (3)$$

Hence the photometric zero point of HRCam in the instrumental I_{HRCam} system is 25.6 mag, and such star gives a flux of 1 el s⁻¹. The instrumental magnitudes can be estimated as

$$I_{\text{HRCam}} \approx G - 0.35(G_{BP} - G_{RP}). \quad (4)$$

A similar comparison of fluxes in the y filter with the V magnitudes of observed stars results in the zero point of 24.6 mag. No color term is necessary because the central wavelengths of the y and V bands are similar. The zero point in the y band is brighter than in I_{HRCam} by 1 mag owing to the smaller bandpass of the green filter.

2.4. Measurement of Binary Stars

Parameters of a binary star (relative position and magnitude difference) are determined by fitting a model to the observed PS $P(\mathbf{f})$:

$$P(\mathbf{f}) \approx P_0(\mathbf{f})[1 - B + B \cos(2\pi\mathbf{f}\mathbf{x})], \quad (5)$$

$$B = 2r/(1 + r^2), \quad (6)$$

$$r = 10^{-0.4\Delta m}, \quad (7)$$

where \mathbf{f} and \mathbf{x} are two-dimensional vectors of the spatial frequency and binary position, respectively, B is the contrast of fringes in the PS which depends on the intensity ratio of the two components r (Tokovinin et al. 2010).

The $P_0(\mathbf{f})$ term is the PS of a single (reference) star. A more general formula for triples is given in Tokovinin (2018). The model is fitted at spatial frequencies between $0.2f_c$ and $0.8f_c$, where $f_c = D/\lambda$ is the cutoff frequency. For relatively wide binaries with separation $\rho \gg \lambda/D$, the reference PS is obtained by angular averaging of the observed PS. Otherwise, a PS of another object observed in the same conditions can be used as a reference (if the reference object is a binary, its fringes are removed by division).

The measurement errors are a quadratic sum of four effects:

1. Random errors of the PS caused by the speckle noise, photon noise, and detector (Section 3.2).
2. Distortions of the single-star PS caused by optical aberrations and vibration, partially accounted for by using a reference star.
3. Atmospheric errors caused by high-altitude turbulence (see their estimate in Tokovinin et al. 2022).
4. Inaccurate calibration of the pixel scale and orientation.

The errors (3) and (4) increase with the binary separation ρ . Analysis of calibrator binaries in Tokovinin et al. (2022) indicates that $\sigma \approx 0.81 + 1.15\rho$ mas, where ρ is in arcseconds. External errors as small as ~ 1 mas were documented by the residuals to good orbits of bright close pairs; residuals are larger for binaries with a large Δm . The random errors are estimated from the formal errors found by fitting the model (5) to the observed PS and from the differences between the results of two data cubes (whichever is larger). They are given in the data tables, and a typical median value is 0.3 mas. Random errors dominate for faint stars; they are studied in Section 3.3.

3. SIMULATIONS

Simulation of speckle data is implemented in IDL (Appendix). It is split into two parts. First, a noiseless data cube is generated. Then, the effect of all noise sources is simulated. This allows us to study the noise using the same input speckle pattern. Real data on a single bright star can be used as well for simulating the noise and optimizing the data processing algorithm. The theory of light propagation through the atmosphere and relevant parameters such as seeing, Fried radius r_0 , and speckle coherence time τ are covered in, e.g., Roddier (1981) and Goodman (1985). Most simulations adopt a seeing of 0.8 at 800 nm which corresponds to $D/r_0 = 20$. The temporal evolution of the speckles is modeled by two

phase screens of equal strength moving with the speeds of 8 m s^{-1} and 40 m s^{-1} in orthogonal directions.

3.1. Effects of Exposure Time and Spectral Bandwidth

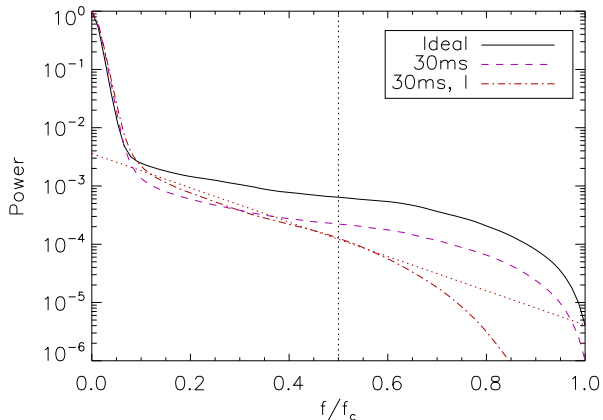


Figure 3. Azimuthally averaged PS of simulated noiseless speckle cubes for a $0''.8$ seeing: an ideal (instantaneous and monochromatic) speckle at 800 nm , a monochromatic exposure of 30 ms (dashed line), and imaging in the I band (dash-dotted). The vertical dotted line marks $0.5f_c$, the red dotted line is a linear approximation of the I -band PS.

The PS of speckle images has two components: the seeing-limited core at low spatial frequencies and the high-frequency part extending up to the cutoff frequency $f_c = D/\lambda$. Only the high-frequency part corresponding to the speckle signal is of interest here. The PS is normalized to one at zero frequency; it is rotationally symmetric. According to the theory, in an ideal speckle pattern the high-frequency part of the PS $P(f)$ should be approximately equal to $0.435(r_0/D)^2 T_0(f)$, where r_0 is the Fried radius at the imaging wavelength and $T_0(f)$ is the diffraction-limited transfer function (Roddier 1981; Goodman 1985); $T_0(0.5) = 0.39$. For $D/r_0 = 20$, we get $P = 4.2 \times 10^{-3}$ at $f = 0.5f_c$. It is convenient to use logarithmic quantities, so the level of the speckle signal (also called speckle contrast) is characterized by the parameter $S = \log_{10} P(0.5f_c)$; in the above numerical example, $S = -3.37$.

Reduction of the speckle contrast due to finite exposure time and wide spectral bandwidth is well understood in theory (Roddier 1981; Tokovinin 1980) and confirmed by measurements (Karo & Schneiderman 1978). The characteristic time of the speckle “boiling” $\tau = r_0/\Delta V$ depends on the turbulence-weighted wind speed dispersion ΔV and is typically a few milliseconds at visible wavelengths. When the exposure time t is significantly longer than τ , the PS is reduced by a factor of τ/t uniformly at all spatial frequencies. A finite spectral bandwidth $\Delta\lambda$ causes radial elongation of the

Table 1. Speckle Signal in Simulations

Case	S	p_0	p_1	FWHM
Ideal	-3.20	-2.81	-0.78	0.69
30 ms	-3.67	-3.19	-0.92	0.63
30 ms, I	-4.03	-2.44	-2.94	0.61

speckle structure reaching $(\Delta\lambda/\lambda)$ (λ/r_0) at the periphery of the image (its radius is λ/r_0). To preserve the speckle contrast, the elongation must be less than the speckle size λ/D , hence the spectral bandwidth is limited to $\Delta\lambda/\lambda < r_0/D$, e.g. 40 nm at $\lambda = 800 \text{ nm}$ and $D/r_0 = 20$. As the bandwidth of the HRCam I filter is wider, the chromatic elongation is nonnegligible, and $P(f)$ is reduced mostly at high spatial frequencies.

Figure 3 shows how the speckle signal is reduced by finite exposure time and wide spectral bandwidth. The same seeing of $0''.8$ was simulated using three different codes of increasing complexity (see Appendix). The $\log_{10} P(f/f_c)$ of the real speckle data is approximated by a straight line between $0.2f_c$ and $0.8f_c$, and these parameters (intercept p_0 and slope p_1) are determined for the simulated data as well. Obviously, $S \approx p_0 + 0.5p_1$. Table 1 lists the PS parameters corresponding to Figure 3. The Full Width at Half Maximum (FWHM) of the simulated average centered images is given in the last column in arcseconds. It is consistent between the simulations and less than the input seeing because the overall image motion has been compensated by centering. We note that the finite exposure time degrades the speckle contrast almost uniformly at all frequencies, while the slope p_1 becomes only slightly steeper; the PS shape resembles $T_0(f)$, as in the monochromatic case. Uniform reduction by a factor of 3 at 30 ms exposure implies a speckle lifetime of $\tau \approx 10 \text{ ms}$. On the other hand, the wide spectral bandwidth degrades mostly the high-frequency speckle power, and the PS becomes steeper compared to the monochromatic light case.

For comparison with simulations, a real image cube EA.009 recorded on January 28, 2021 was selected. This corresponds to a bright reference star observed in the I filter with an effective exposure time of 27.8 ms . The seeing was relatively good, and the average image is almost round with a FWHM of $0''.69$. Figure 4 compares the real and simulated speckle PS. The values of S match almost exactly. The FWHM of the average (centered and coadded) simulated image is $0''.61$; it is smaller than the simulated seeing of $0''.80$ owing to the centering (tilt compensation). The real image is slightly larger, but it shows signs of residual aberrations (note a small “tail” marked by the red arrow).

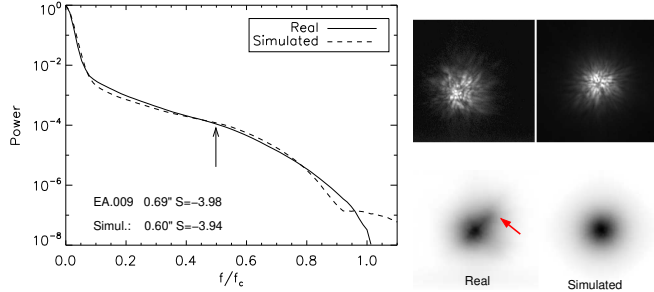


Figure 4. Comparison between real and simulated data in the I filter. Left: PS averaged in angular coordinate; right: individual speckle images (top) and the average images in negative rendering (bottom). Note that the linear fit to PS between 0.2 and $0.8 f_c$ (not plotted) is a poor approximation in this case.

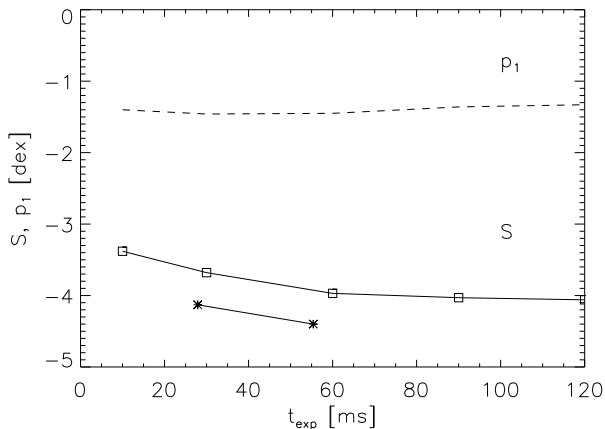


Figure 5. Dependence of the speckle signal S (solid line and squares) and the PS slope p_1 (dashed line) on the exposure time according to simulations. Asterisks show results for the real image cube EA.009.

Simulations help us to optimize the exposure time of individual frames. With increasing exposure, a larger number of photons from the star is collected, but at the same time, the speckle signal S is reduced. The effect of increasing exposure time is explored in Figure 5. An exposure increase from 30 to 60 ms reduces the speckle signal S by 0.3 dex (by a factor of 2). This reduction is almost uniform at all spatial frequencies, so the slope p_1 remains approximately constant (see the dashed line in Figure 3). Asterisks show results for the real image cube EA.009 and for the cube with frames binned (averaged) pairwise. Binning of frames reduces the speckle signal from -4.13 to -4.40 dex, also by a factor of 2.

Figure 6 shows how the level of the speckle signal in the I filter degrades with increased seeing. The slope p_1 also becomes steeper, mostly owing to the finite spectral bandwidth.

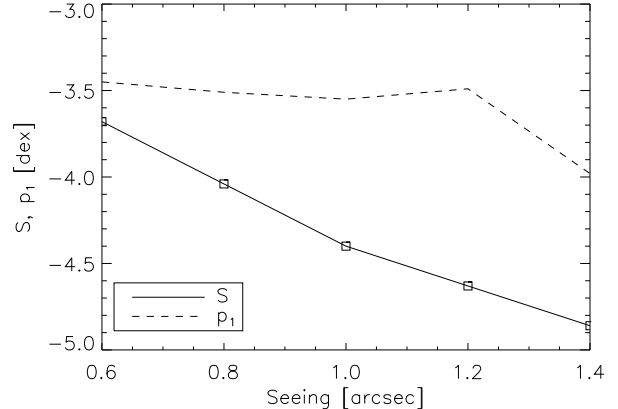


Figure 6. Dependence of the speckle signal S (solid line and squares) and the PS slope p_1 (dashed line) on seeing. Simulations with a 30 ms exposure time and the I filter.

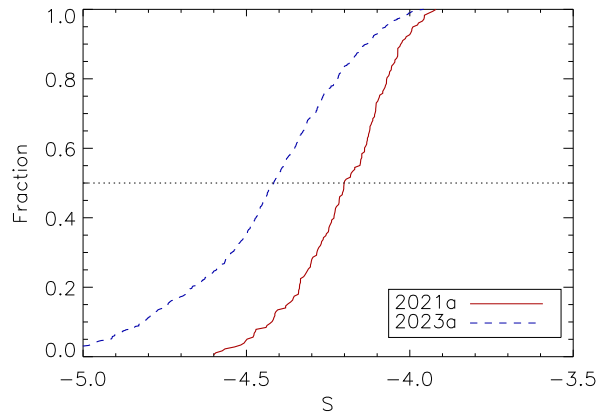


Figure 7. Cumulative histograms of the speckle signal S in the I filter without binning in the speckle runs of 2021a and 2023a with good and average seeing, respectively. The median S values are -4.19 and -4.42 and the median PS slopes p_1 are -3.78 and -3.61 .

Cumulative histograms of the actual speckle signal S in two observing runs are shown in Figure 7. Note that the standard processing algorithm with double clipping slightly biases S to smaller values, and this bias depends on the number of detected photons per frame N_{ph} , as demonstrated by processing simulated data with single and double clipping. Double clipping has little effect on bright stars.

Compared to the simulations, the speckle signal in the real data may be reduced by additional factors such as optical aberrations (e.g. imperfect focusing) and telescope vibration. The reasonably good match between real data and simulations is encouraging, suggesting that these additional degrading factors play a minor role. The atmospheric parameters adopted in the simulations (e.g. the wind speed) differ from the actual (unknown) parameters. Approximate agreement with the real data

justifies the use of these simulations for evaluation of the HRCam performance.

3.2. *Signal-to-noise Ratio and Limiting Magnitude*

The noise simulator reads a simulated noiseless image cube from a fits file, generates pixel values affected by the detector noise and random numbers of photons, computes the PS, and determines its relevant parameters. The amplification noise in an EM CCD is also simulated: each photon generates a random signal distributed as a negative exponent with a decrement A which equals the average amplitude of single-photon events, and randomly amplified signals of all photons in a pixel are summed up. The photon numbers in each pixel follow the Poisson distribution with an average value equal to the sum of the stellar photons and CIC. Simulating the HRCam detector with $E_g = 100$, I adopt $A = 10$ and a CIC rate of 0.02. A threshold of 10 ADU is used in the PS calculation.

If a perfect detector records N_{ph} photon events per frame on average, the PS increases by $P_{\text{bias}} = 1/N_{\text{ph}}$ at all frequencies owing to the photon noise bias (Goodman 1985). This theoretical result has been reproduced in the simulation. The value of P_{bias} is evaluated by averaging the PS over frequencies beyond f_c , where the speckle power is zero. The bias is subtracted from the PS before its azimuthal averaging and model fitting. Additional noise sources increase the PS bias, reducing the effective number of photons, and this reduction factor $1/(P_{\text{bias}}N_{\text{ph}})$ is a convenient dimensionless characteristic of the sensitivity loss caused by a noisy detector in comparison with an ideal one.

For bright stars, the photon noise should dominate over the detector noise, and the relation $P_{\text{bias}} = 1/N_{\text{ph}}$ should hold. So, the measured values of P_{bias} can be used to estimate N_{ph} and, by comparing it with the recorded flux, to check g , the conversion factor of the detector. Analysis of the HRCam data revealed that the flux recorded in the database was strongly reduced by double clipping (see above). With the correct (re-computed) fluxes, the expected linear relation between P_{bias} and $1/N_{\text{ph}}$ is retrieved, leading consistently to the gain factor $g = 4.7 \text{ e-/ADU}$, 2 times less than measured. The reason for this apparent discrepancy is the amplification noise. It doubles the signal variance, compared to a pure Poisson distribution, and effectively halves N_{ph} . Simulation of an EM CCD with amplification noise indeed shows that $P_{\text{bias}} = 2/N_{\text{ph}}$. So, the HRCam data are consistent with simulations. For bright stars, where the speckle noise dominates anyway, the SNR loss due to the amplification noise is not detrimental, but it matters for faint stars, as well as CIC.

For one frame, the variance of the FT square modulus at each spatial frequency equals the square of its mean value (this is a consequence of the negative-exponential distribution of the square modulus). Averaged over N_z frames, the relative rms fluctuations of the PS equal $1/\sqrt{N_z}$ (Dainty 1974). Let 10^S be the value of the speckle power at half of the cutoff frequency, identified with the useful signal. The total PS signal is $10^S + P_{\text{bias}}$, so the SNR in one element of the PS is

$$\text{SNR} = \sqrt{N_z} 10^S / (10^S + P_{\text{bias}}). \quad (8)$$

For bright stars, $10^S \gg P_{\text{bias}}$, the speckle noise dominates, and the SNR tends to 20 for $N_z = 400$. For faint stars, P_{bias} becomes the dominant term in the PS and determines the SNR. The transition between the bright-star and faint-star regimes depends on the level of the speckle signal S , it is around $N_{\text{ph}} \sim 10^4$ for $S = -4$.

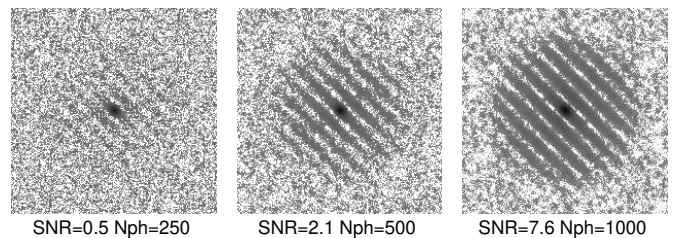


Figure 8. Power spectra of a simulated binary star with equal components displayed on a negative logarithmic scale. The SNR and N_{ph} are indicated. An EM CCD with CIC=0.02, $A = 10$, and threshold of 10 ADU is simulated. An ideal speckle data cube was used as input.

Optionally, a binary star can be simulated by adding a shifted copy of the speckle pattern scaled by the binary intensity ratio before simulating the noise. Figure 8 shows fringes in the PS of a binary star at different photon fluxes. Note that the SNR parameter here refers to single stars (fringes reduce the average level of the PS and further decrease the SNR). At an SNR of 0.5, the fringes are almost lost in the fluctuations of the photon noise bias, but the binary can still be detected and measured (Section 3.3).

With realistic simulations of the noisy speckle data, I explore the combined effect of the seeing variation and the source flux on the SNR (Figure 9). The instrumental I magnitudes of stars that reach SNR=1 range from 11.5 to 14.5 mag, depending on the seeing. These estimates are slightly optimistic because, compared to the simulation, the speckle contrast is additionally reduced by imperfect optics (e.g. a focus error) and by telescope vibration. On the other hand, a slower wind in the upper atmosphere would increase S and the magnitude limit relative to the simulations. Doubling the exposure time

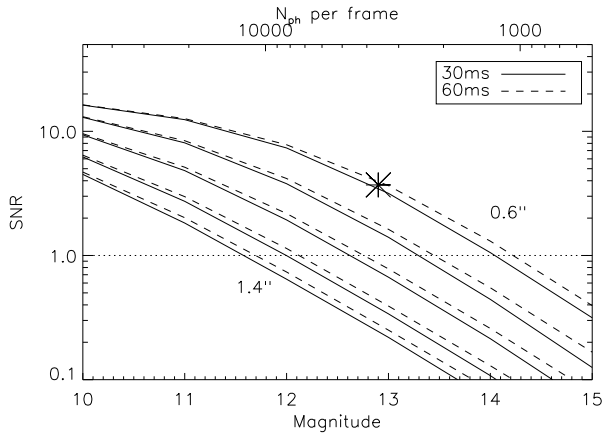


Figure 9. Signal-to-noise ratio in the simulated HRCam with an EM CCD detector vs. stellar magnitude in the instrumental system I . Full lines and upper axis correspond to the 30 ms exposure, and dashed lines correspond to the 60 ms exposure, both with 400 frames per data cube. The curves are computed for seeing values of 0.6, 0.8, 1.0, 1.2, and 1.4 arcsecond. The asterisk shows the observation of V1311 Ori D in 2021.7983 (see text).

from 30 to 60 ms doubles the flux N_{ph} , but reduces the speckle power by the same amount (in agreement with the theory), so the small net SNR gain is due to secondary factors like CIC; it comes at the cost of doubling the acquisition time.

As a real example, consider observation of the faint single red dwarf V1311 Ori D reported in Tokovinin (2022). On that date, 2021.7983, the seeing was very good. The FWHM of the centered image in the data cube EK.026 (exposure time 50 ms) is $0''.63$, the estimated speckle signal is $S = -3.7$, and the SNR is 3.7. With the instrumental magnitude of 12.92, estimated from the $G = 13.92$ mag and the color $G_{BP} - G_{RP} \approx 2.4$ mag, the experimental point (asterisk) falls near the upper curves in Figure 9. Note that for very red stars, the effective spectral response differs from the response assumed in the simulation.

3.3. Dependence of Measurement Errors on the SNR

Measurement of the binary stars' parameters (relative position and magnitude difference) depends on the random and systematic errors of the PS. Most observed binary stars are bright, and the systematic errors dominate (Section 2.4). The influence of systematic errors is reduced by observations of a reference star under the same conditions, provided that the instrument-related PS distortions are stable. An example of erroneous measurement caused by vibration is given in Figure 6 in Tokovinin (2018).

For faint stars, random errors dominate, and they can be quantified by simulations. I simulated a binary star

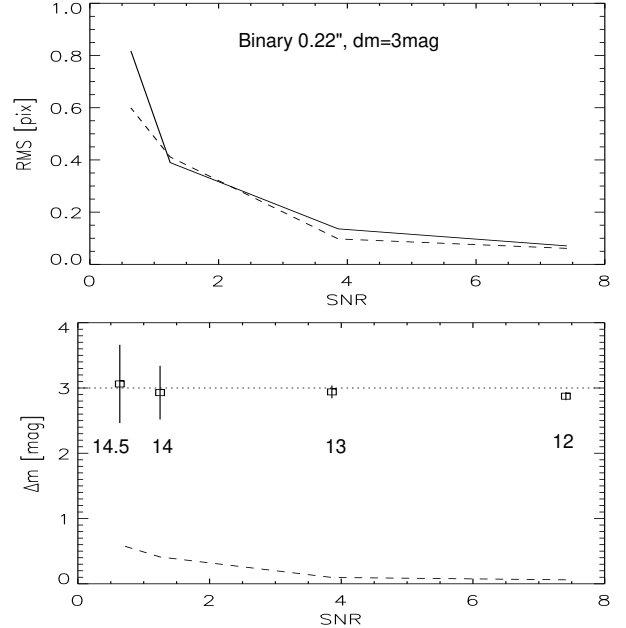


Figure 10. Errors in the position (top: the solid and dashed lines correspond to two orthogonal directions) and magnitude difference (bottom) of simulated binary star measurements depending on the SNR. Approximate magnitudes are indicated in the lower plot, where the dashed line shows the errors, while squares with error bars show the mean fitted Δm and their scatter.

with a separation of $0''.22$ and a magnitude difference $\Delta m = 3$ mag with combined magnitude ranging from 12 to 14.5 mag, observed with HRCam under standard conditions in the I filter. For each magnitude, 20 random noisy cubes were generated, and a binary star model was fitted to the PS. Figure 10 plots the results. The SNR varies between 0.6 and 7.5. The relative flux of the companion is only 0.063, and the fringe contrast in the PS is 0.126. Despite this, the model fits to the PS do not diverge even at an SNR of 0.6 (remember that SNR is defined at one spatial frequency, while the parameter fit uses all frequencies between $0.2f_c$ and $0.8f_c$). The position errors reach 0.7 pixels or 11 mas.

4. COMPARISON BETWEEN EM CCD AND CMOS DETECTORS

Recently, the noise level of CMOS detectors has improved to the point where they have become competitive with EM CCDs. CMOS detectors for astrophotography, e.g. ASI462 from ZWO,² are very cheap and readily available, while their RON is about 0.5 e-. Hamamatsu developed a scientific qCMOS camera ORCA Quest with

² <https://www.zwoastro.com/product/asi462mm/>

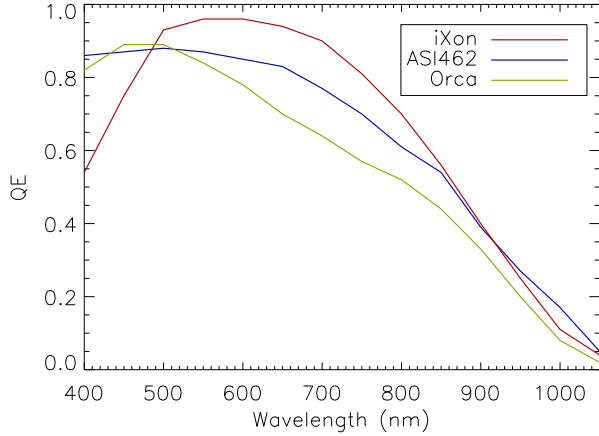


Figure 11. Quantum efficiency of three detectors for speckle interferometry according to the vendor’s data: EM CCD iXon X3 888 from Andor, ASI462 from ZWO, and ORCA-Quest from Hamamatsu.

a subelectron RON.³ Its indicative cost is \$50K. This Hamamatsu camera has been installed in the speckle interferometer of the 2.5 m telescope and demonstrated an improvement in limiting magnitude (Strakhov et al. 2023). A CMOS detector, even with a 0.5 e⁻ RON, eliminates such problems of EM CCDs as CIC and amplification noise. The quantum efficiency of these three detectors is comparable (Figure 11).

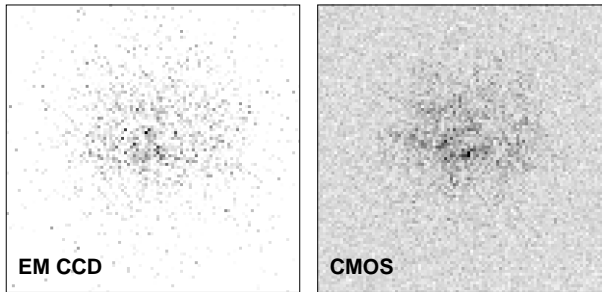


Figure 12. Simulated single noisy frames with $N_{\text{ph}} = 3000$ corresponding to an EM CCD (left, SNR=1.7), and a CMOS with RON=0.5 e⁻ (right, SNR=3.3). The central region of 100×100 pixels is shown in negative linear stretch.

These detectors are compared below by additional simulations. The amplification noise and CIC are both absent for CMOS. I assume a RON of 0.5 e⁻, i.e. a cheap CMOS camera. The EM CCD parameters are the same as above. Figure 12 compares simulated speckle images of a faint source with the same $N_{\text{ph}} = 3000$ corresponding to these detectors (I filter, 30 ms exposure time, $S = -4$ dex).

³ <https://www.hamamatsu.com/us/en/product/cameras.html>

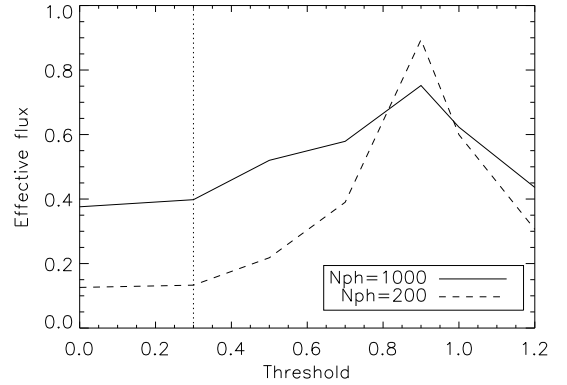


Figure 13. Effective loss of flux $1/(P_{\text{bias}}N_{\text{ph}})$ vs. threshold for a qCMOS with RON of 0.3 e⁻ (marked by the vertical dotted line) and for two levels of the flux.

Signal clipping in the calculation of the PS is needed for a CMOS to reduce the impact of RON in “empty” pixels that do not contain stellar photons. Figure 13 shows the effective flux loss vs. threshold for a low-noise qCMOS camera and two levels of photon flux. The optimum threshold appears to be near $3\times\text{RON}$. For a CMOS with a RON of 0.5 e⁻, the same 3σ threshold is adopted. It seems that clipping has not been used by Strakhov et al. (2023), who found a smaller gain in sensitivity when switching from an EM CCD to a qCMOS. Note also that their EM CCD has a higher level of CIC events compared to HRCam (0.04 vs. 0.02).

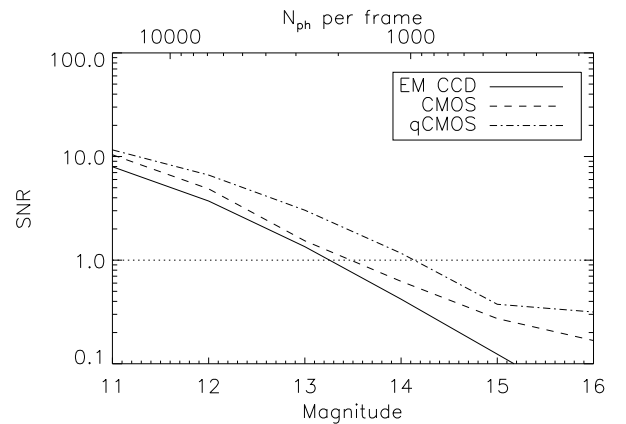


Figure 14. Signal-to-noise ratio (SNR) in the PS at half of the cutoff frequency vs. magnitude in the I band for a 0.8 seeing and three simulated detectors: an EM CCD, a scientific CMOS (RON of 0.5 e⁻), and a qCMOS (RON of 0.3 e⁻). The upper axis gives the number of photons per frame in a 30 ms exposure; the SNR assumes 400 frames per data cube.

Figure 14 compares the SNR vs. magnitude for the three detectors. It assumes equal N_{ph} and an optimized

threshold in the PS calculation. A realistic level of the speckle signal $S = -4$ dex corresponding to a $0''.8$ seeing and an I filter is adopted (see Figure 6). An upgrade from an EM CCD to a qCMOS offers a sensitivity gain of ~ 1 mag. Note that the SNR is computed for $N_z = 400$. Increasing the number of acquired frames by a factor of 10 pushes the curves up by a factor of 3, and 16th mag stars become accessible with a qCMOS.

The SNR plot in Figure 14 refers to the speckle signal at $0.5f_c$. In a wide spectral band like I , the PS has a steep slope, and its value at $0.2f_c$ is larger by almost an order of magnitude, $S \sim -3$ dex (Figure 3). So, speckle observations of faint stars are feasible at a reduced spatial resolution, and there is an obvious trade-off between resolution and sensitivity.

Although the CCDs and CMOS detectors are linear, the speckle signal processing involves two nonlinear operations: clipping and PS calculation. The PS is proportional to the square of the signal, and an additive background such as CIC events is no longer additive in the PS. A numerical experiment was conducted to evaluate the effect of signal processing on the relative photometry of a binary star with a magnitude difference of 1 mag. The result is reassuring. Even in the conditions of $\text{SNR} < 1$, when the fringes are barely seen (Figure 8), no systematic trend in the estimated Δm is present for both an EM CCD and a qCMOS. In Figure 10, the input $\Delta m = 3$ mag is also retrieved without bias. A minor bias is expected at $\Delta m \approx 0$ because the measured fringe contrast B becomes independent of the flux ratio: $dB/dr = 0$ at $r = 1$.

5. TOWARD AUTOMATED OBSERVATIONS?

Speckle observations are a complex process. It starts with the preparation of the program for each observing run. Merging all active projects into a common program has many advantages and increases the overall efficiency, compared to the classical by-program telescope use. A common set of calibrators, for example, ensures consistent calibration for all projects. Brighter binaries can be measured under poor seeing, when fainter (and higher-priority) targets would not yield useful data anyway (they can be pointed on another night with better seeing). So, the observing program always includes more objects than can be observed on a given night, maximizing the use of allocated telescope time.

The outcome of each observation depends on the current conditions, mostly on the seeing and transparency. Factors such as telescope shake are important on windy nights, restricting the pointing direction. So, the selection of targets is managed flexibly in real time, balancing between priorities, target visibility, and current condi-

tions while optimizing the telescope slews. Quick online calculation of the PS helps the observer to evaluate the HRCam performance and to adjust the target choice accordingly. For example, if a source is resolved into a new tight binary, observation of a reference star immediately after is needed for a correct data reduction.

Considering this inherent complexity of speckle observations and the need to make real-time decisions based on several variables, it will be difficult to substitute an experienced observer with an automatic process. The study done here helps this task in several ways, allowing to replace subjective evaluation of the observing conditions and the data quality with quantitative metrics such as N_{ph} , S , and SNR. Simulations will help us to define reasonable performance goals and acceptable SNR for each target; this will set the stage for automating observations in the future. The automation should be gradual, starting from sequencing routine actions and progressing toward robotic operation under human supervision. Given current conditions and constraints, the observer can define a sequence of several targets for which the data will be taken robotically. This will speed up the data acquisition and increase the overall efficiency. On the other hand, the quality of the data acquired robotically may be worse.

Processing of the observations acquired on a speckle night starts by running a pipeline that computes the PSs and the associated data products, as described in Tokovinin (2018). Manual inspection of the data and fitting binary parameters is relatively quick; it takes less than a half of the telescope time used to acquire the data, and about as much time is spent on the subsequent analysis of the results. Experience helps to distinguish real binary companions from artifacts and to resolve difficult cases (binaries with small separations and large contrast and triples). In principle, a suitably trained neural network can handle this task if the large data volume makes their processing by humans prohibitive.

The results of observations are incorporated into the observing program and used to decide on the next observations. For example, a rapid orbital motion calls for repeated measurements within a year or even sooner. Thus, the process program \rightarrow observations \rightarrow program is circular, with a rapid feedback. This differs from the classical open-ended approach where the data analysis sometimes is performed several years after their acquisition.

6. SUMMARY

The large volume of HRCam speckle data accumulated to date warrants the analysis of their quality performed here. Parameters of the current EM CCD detec-

tor and the photometric calibration that relates source magnitude to the number of detected photons allow a fair comparison between the actual level of the speckle signal S and the SNR to those expected under typical seeing conditions. For the latter, I adopted a simplified model consisting of two turbulent layers moving at different speeds. The parameters of the model are adjusted to match typical data. Simulations help us to quantify the effects of finite exposure time and spectral bandwidth, to predict the dependence of the SNR on seeing and stellar magnitude, and verify that the algorithm of PS calculation with clipping is quasi-optimal. I consider here only the wide-band I filter used for observations of faint stars.

The main results of this study are summarized below.

- The photometric zero points of HRCam corresponding to a detected flux of one $e^- s^{-1}$ in the I and y filters are 25.6 and 24.6 mag, respectively. The relation of the instrumental I magnitudes to the Gaia photometry is established.
- The IDL code for simulating speckle images, including the detector noise, is developed and made available.
- In the calculation of the PS, signal clipping is necessary for maximizing sensitivity with both an EM CCD and a CMOS. For the latter, the optimum clipping threshold is 3 times the RON. Signal clipping does not spoil the relative photometry of binary stars.
- The speckle PS decreases uniformly at all frequencies with increasing exposure time. However, in the wide I band, the speckle contrast declines with spatial frequency faster than in monochromatic light (Figure 4). The level of the speckle signal

is quantified by S , the decimal logarithm of the PS at half of the cutoff frequency. Under good conditions, $S \approx -4$ in the I filter.

- Increasing the exposure time from 30 to 60 ms does not increase the SNR in the PS but doubles the acquisition time. For faint stars, it is better to acquire a larger number of short-exposure frames.
- Measurements of faint binary stars are possible at SNR ~ 1 . With the current EM CCD, this corresponds to the I magnitude from 11.5 to 14 mag for the seeing from $1''.4$ to $0''.6$ (Figure 9). A sensitivity gain of at least 1 mag is expected with a low-noise CMOS detector (Figure 14). A CMOS detector overcomes two major limitations of an EM CCD, namely the CIC background and the amplification noise.
- Quantitative characteristics of the HRCam performance and relations between seeing conditions, SNR, and measurement errors will help to plan and execute speckle observations and, eventually, to automate them in the future.

Although this study is devoted to the HRCam imager at SOAR, its results may be useful for optimizing the performance of other speckle instruments. For example, speckle observations in a wide band on a 4 m telescope are discussed by Clark et al. (2024). An upgrade from EM CCD to CMOS is recommended for the current and future speckle imagers.

The Andor EM CCD camera was loaned to SOAR in 2017 by N. Law from the University of North Carolina, resulting in a significant sensitivity gain compared to the previously used detector. I thank B. Mason and the anonymous Referee for useful comments on this manuscript.

APPENDIX

A. SIMULATION CODE

The IDL code `simspec4.pro` simulates a realistic speckle data cube for the 4.1 m SOAR telescope. The monochromatic image of a star at wavelength λ is computed in the standard way as a square modulus of the FT of the light-wave amplitude at the telescope pupil (e.g. Roddier 1981; Goodman 1985). The size of the computing grid N , 200×200 , and the angular pixel scale $p = 0''.01575$, are chosen to match the real data. The physical size of the grid in the pupil space equals $L = \lambda/p$ (10.5 m for $0.8 \mu\text{m}$, or 0.05 m per spatial pixel). This sets the pupil radius in pixels; the central obstruction (0.25 fraction of pupil diameter) is also emulated in constructing the pupil mask. Figure 15 helps to visualize the geometry of simulations.

The random atmospheric phase perturbations obeying Kolmogorov statistics (Roddier 1981) are generated using the standard Fourier method (Lane et al. 1992), given the Fried parameter $r_0 = 0.98\lambda/\epsilon$ for the seeing ϵ (in radians).

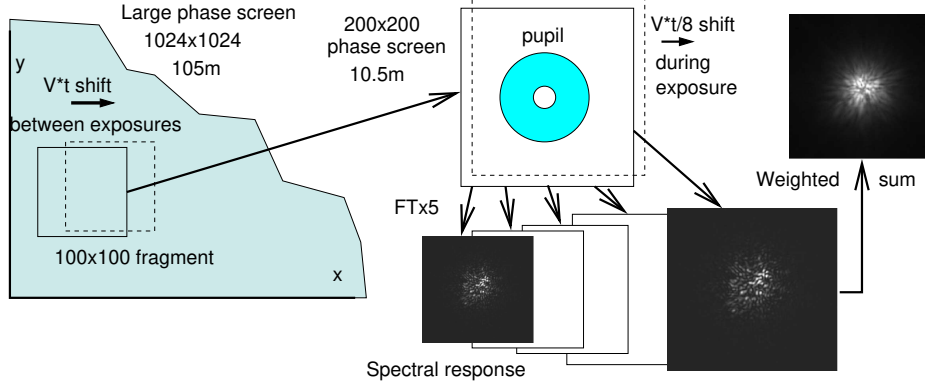


Figure 15. Scheme of the speckle simulation code (see text).

In the simplest version of the code, the same pupil space grid was used to compute the phase screens. However, to simulate the effects of the finite exposure, the phase screens of 1024×1024 size with twice larger pixels (physical screen size 105 m) are generated. The pupil grid corresponds to a 100×100 pixel fragment of the large screen, and it is interpolated on a finer 200×200 grid for the image calculation.

To simulate temporal evolution of the speckle pattern, at each successive frame, the origin of the selected fragment of the large phase screen is translated horizontally (in X) by Vt , where V is the wind speed and t is the exposure time (e.g. 1.2 m for $V = 40 \text{ m s}^{-1}$ and $t = 0.03 \text{ s}$). The translation is rounded to an integer number of pixels. Orthogonal shifts are applied at every 10th translation in order to sample the full large screen, so the fragment’s motion is in fact tilted with respect to the X axis by $1/10$ radian (5.7°). When the selected fragment reaches the edge of the large screen, it “rolls over” in both coordinates without discontinuity (the phase screens are doubly periodic owing to their generation method).

The phase perturbation at the telescope pupil is produced by several turbulent layers moving at different speeds, and the temporal evolution of the speckle is governed mostly by the changing phase sum rather than by the overall translation over the pupil. So, two phase screens are generated. One is translated in X with a speed of 8 m s^{-1} , another in Y with a speed of 40 m s^{-1} . The turbulence intensity is equally distributed between these screens. For a seeing of $0.8''$, this layout corresponds to the atmospheric time constant (see definition in [Roddier 1981](#)) of 1.3 ms at 500 nm. All parameters in the code can be easily modified.

To reproduce the image smearing during exposure, the latter is split into 8 steps. The two phase-screen fragments selected for a given exposure and re-binned on a 200×200 grid are shifted during the exposure by small steps of $Vt/8$ in the orthogonal directions. At each step, the speckle image is computed, and each frame of the image cube is the average of these eight images. For the following frame, new fragments are cut out from the large phase screens.

Simulation of speckles in a wide bandwidth adds another layer of complexity. The spectral response of HRCam in the I filter is modeled by a combination of 5 wavelengths λ_i from 0.75 to $0.90 \mu\text{m}$ with relative weights of $[0.724, 0.694, 0.539, 0.347, 0.190]$ — product of the filter transmission and the detector response (see Figure 2 in [Tokovinin 2018](#)). The effective wavelength is $0.822 \mu\text{m}$. The actual response depends on the spectrum of the star, of course.

For each of the 8 subframes, we compute five images corresponding to λ_i and combine them with relative weights defined by the spectral response. So, calculation of one speckle frame requires $8 \times 5 = 40$ FTs, and the simulation of the image cube takes about 45 s. The wave front distortion Δl in linear units corresponds to a wavelength-dependent phase shift of $\Delta\phi = 2\pi\Delta l/\lambda$. So, the phase perturbation, defined for the reference wavelength λ_0 , is scaled by the factor $a = \lambda_0/\lambda_i$. However, this is not sufficient because the pupil size and the computing grid are dimensioned for λ_0 , not for λ_i . This is accounted for by stretching each monochromatic image by the factor $1/a$ (at longer wavelengths, the speckles become larger). The same effect could be achieved by shrinking the phase pattern and the pupil function by a factor a before calculating the image by FT. As a check, suppose that the phase aberration is linear (a pure tilt). Scaling it by $a < 1$ reduces the tilt and moves the image closer to the field center. Stretching the image by $1/a$ times moves it back to the original position, so the tilt becomes achromatic, as expected. Speckles in the simulated polychromatic images are extended radially, as in the real images, while the image moves as a whole owing to random tilts.

The noiseless image cube (either simulated or real) serves as input to the general-purpose noise simulator `noisesimul.pro`. As the simulator does not “know” the wavelength, telescope diameter, and pixel scale, the cut-off frequency f_c (in pixels) must be provided at input. The number of photons per frame N_{ph} sets the detected flux from the star. The noise simulation algorithm is described below; it is implemented by the following piece of IDL code relevant to one frame:

```
tmp = cube[*,*,i] ; noiseless speckle image
if keyword_set(binary) then tmp += binary[2]*shift(tmp, binary[0], binary[1])
tmp = tmp/total(tmp)*Nph ; normalize by average photon number
for k=0,nx-1 do for l=0,nx-1 do begin ; loops over nx*nx pixels
  npix = randomn(seed, poisson=tmp[k,l]+CIC) ; number of events in pixel
  if (ampl gt 1) then begin ; EM CCD, amplification noise
    s = 0 & if (npix gt 0) then for j=0,npix-1 do s += -alog(randomu(seed))
    ncube[k,l,i] = ampl*s + ron*randomn(seed) ; EM CCD
  endif else ncube[k,l,i] = npix + ron*randomn(seed) ; CMOS
endfor ; pixel loop
```

Each frame `tmp` is normalized to a unit sum and multiplied by N_{ph} to get the expected photon numbers in each pixel. This number serves to generate the actual random number of photons `npix` after adding the CIC probability (the Poisson random number generator is used). For a CMOS detector, $\text{CIC}=0$, and the pixel value equals `npix` plus a Gaussian RON, which must be specified in electrons. For an EM CCD, each photon is “amplified” to an average level `Ampl` (in ADU) with a negative-exponential distribution, and the resulting pixel signal is a sum of all randomly amplified photons. This simulates the amplification noise. The readout noise is also simulated, but for an EM CCD it should be specified in ADUs rather than in electrons. The amplification step is skipped for a CMOS by setting `Ampl=1`. Simulated noisy speckle images are illustrated in Figure 12. The speckle simulation code is available at <https://www.ctio.noirlab.edu/~atokovin/speckle/simulation.html> and on Zenodo (Tokovinin 2024).

Facility: SOAR

REFERENCES

- Clark, C. A., van Belle, G. T., Horch, E. P., et al. 2024, *AJ*, 167, 56, doi: [10.3847/1538-3881/ad0bfd](https://doi.org/10.3847/1538-3881/ad0bfd)
- Dainty, J. C. 1974, *MNRAS*, 169, 631, doi: [10.1093/mnras/169.3.631](https://doi.org/10.1093/mnras/169.3.631)
- Davidson, J. W., Horch, E. P., Majewski, S. R., et al. 2024, *AJ*, 167, 117, doi: [10.3847/1538-3881/ad1ff6](https://doi.org/10.3847/1538-3881/ad1ff6)
- Gaia Collaboration, Brown, A. G. A., Vallenari, A., et al. 2021, *A&A*, 649, A1, doi: [10.1051/0004-6361/202039657](https://doi.org/10.1051/0004-6361/202039657)
- . 2016, *A&A*, 595, A2, doi: [10.1051/0004-6361/201629512](https://doi.org/10.1051/0004-6361/201629512)
- Goodman, J. W. 1985, *Statistical optics* (New York, Wiley-Interscience)
- Horch, E. P., Veillette, D. R., Baena Gallé, R., et al. 2009, *AJ*, 137, 5057, doi: [10.1088/0004-6256/137/6/5057](https://doi.org/10.1088/0004-6256/137/6/5057)
- Karo, D. P., & Schneiderman, A. M. 1978, *Journal of the Optical Society of America*, 68, 480
- Labeyrie, A. 1970, *A&A*, 6, 85
- Lane, R. G., Glindemann, A., & Dainty, J. C. 1992, *Waves in Random Media*, 2, 209, doi: [10.1088/0959-7174/2/3/003](https://doi.org/10.1088/0959-7174/2/3/003)
- Mason, B. D., Tokovinin, A., Mendez, R. A., & Costa, E. 2023, *AJ*, 166, 139, doi: [10.3847/1538-3881/acedaf](https://doi.org/10.3847/1538-3881/acedaf)
- Mitrofanova, A., Dyachenko, V., Beskakotov, A., et al. 2021, *AJ*, 162, 156, doi: [10.3847/1538-3881/ac1a78](https://doi.org/10.3847/1538-3881/ac1a78)
- Roddier, F. 1981, *Progress in Optics*, 19, 281, doi: [10.1016/S0079-6638\(08\)70204-X](https://doi.org/10.1016/S0079-6638(08)70204-X)
- Scott, N. J., & Howell, S. B. 2018, in *Society of Photo-Optical Instrumentation Engineers (SPIE) Conference Series*, Vol. 10701, *Optical and Infrared Interferometry and Imaging VI*, ed. M. J. Creech-Eakman, P. G. Tuthill, & A. Mérand, 107010G, doi: [10.1117/12.2311539](https://doi.org/10.1117/12.2311539)
- Scott, N. J., Howell, S. B., Gnilka, C. L., et al. 2021, *Frontiers in Astronomy and Space Sciences*, 8, 138, doi: [10.3389/fspas.2021.716560](https://doi.org/10.3389/fspas.2021.716560)
- Strakhov, I. A., Safonov, B. S., & Cheryasov, D. V. 2023, *Astrophysical Bulletin*, 78, 234, doi: [10.1134/S1990341323020104](https://doi.org/10.1134/S1990341323020104)
- Tokovinin, A. 1980, *Soviet Astronomy Letters*, 6, 386
- . 2018, *PASP*, 130, 035002, doi: [10.1088/1538-3873/aaa7d9](https://doi.org/10.1088/1538-3873/aaa7d9)
- . 2022, *AJ*, 163, 127, doi: [10.3847/1538-3881/ac4bc5](https://doi.org/10.3847/1538-3881/ac4bc5)
- . 2023, *AJ*, 165, 180, doi: [10.3847/1538-3881/acc464](https://doi.org/10.3847/1538-3881/acc464)

—. 2024, Simulation of speckle data, 1.0, Zenodo,
doi: [10.5281/zenodo.12666756](https://doi.org/10.5281/zenodo.12666756)

Tokovinin, A., & Cantarutti, R. 2008, PASP, 120, 170,
doi: [10.1086/528809](https://doi.org/10.1086/528809)

Tokovinin, A., Mason, B. D., & Hartkopf, W. I. 2010, AJ,
139, 743, doi: [10.1088/0004-6256/139/2/743](https://doi.org/10.1088/0004-6256/139/2/743)

Tokovinin, A., Mason, B. D., Mendez, R. A., & Costa, E.
2022, AJ, 164, 58, doi: [10.3847/1538-3881/ac78e7](https://doi.org/10.3847/1538-3881/ac78e7)